

Hydrothermal Synthesis and Electrochemical Performances of Ag-coated Nanoflake-like $\text{Li}_4\text{Ti}_5\text{O}_{12}$ as an Anode Material for Lithium-ion Batteries

Ying Zhang, Fan Zhang*, Jun Li*, Qi Yang

School of Materials Engineering, Shanghai University of Engineering Science, Shanghai 201620, China

*E-mail: zhangf416@gmail.com, jacob_lijun@sues.edu.cn

Received: 11 November 2020 / Accepted: 4 January 2021 / Published: 31 January 2021

The inherent low electronic conductivity of $\text{Li}_4\text{Ti}_5\text{O}_{12}$ leads to a lower capacity and poor rate performance under high current charge/discharge conditions, which causes serious polarization of the lithium-ion battery. In this work, a $\text{Li}_4\text{Ti}_5\text{O}_{12}$ precursor was prepared by a hydrothermal method, and Ag-modified materials with different Ag contents of 0 wt.%, 3 wt.%, 5 wt.%, 7 wt.% and 9 wt.% were prepared by one-step calcination at 600 °C. The characterization of composite materials was performed through XRD, SEM, TEM, and XPS. Electrochemical tests, such as constant current charge and discharge, cycle performance, rate performance, cyclic voltammetry and electrochemical impedance spectroscopy tests, were also conducted to check the electrochemical performances of Ag-modified materials. The results show that the $\text{Ag@Li}_4\text{Ti}_5\text{O}_{12}$ composite has better electrochemical performance than pristine $\text{Li}_4\text{Ti}_5\text{O}_{12}$. Under a current density of $32 \text{ mA}\cdot\text{g}^{-1}$, the discharge specific capacity of pristine $\text{Li}_4\text{Ti}_5\text{O}_{12}$ reaches $160.35 \text{ mAh}\cdot\text{g}^{-1}$ during the first cycle while the $\text{Ag@Li}_4\text{Ti}_5\text{O}_{12}$ composite with 7 wt.% Ag exhibits a higher value of $256.75 \text{ mAh}\cdot\text{g}^{-1}$. Moreover, its high-rate capacity at $1600 \text{ mA}\cdot\text{g}^{-1}$ is greatly enhanced from $102.91 \text{ mAh}\cdot\text{g}^{-1}$ to $146.56 \text{ mAh}\cdot\text{g}^{-1}$ after Ag modification. It is proven that the addition of an appropriate amount of Ag can increase not only the extraction and insertion of lithium ions but also the diffusion coefficient of lithium ions, which can reduce electrode polarization and improve the conductivity of the material. The conductivity of the $\text{Ag@Li}_4\text{Ti}_5\text{O}_{12}$ composite with 7 wt.% Ag is $1.833\times 10^{-5} \text{ S}\cdot\text{cm}^{-1}$, which is much higher than that of pristine $\text{Li}_4\text{Ti}_5\text{O}_{12}$ ($6.399\times 10^{-6} \text{ S}\cdot\text{cm}^{-1}$), making $\text{Ag@Li}_4\text{Ti}_5\text{O}_{12}$ a promising high-performance anode material.

Keywords: hydrothermal method, anode material, Ag modification, $\text{Ag@Li}_4\text{Ti}_5\text{O}_{12}$ composite

1. INTRODUCTION

Lithium-ion batteries (LIBs) have now become one of the first choices for most portable electronic devices. Choosing appropriate electrode materials is the key to improving the performance of

lithium-ion batteries [1]. For anode materials, graphite is commonly used in LIBs. However, when this kind of battery is overcharged, lithium dendrites will form due to the precipitation of metallic lithium on the surface of the graphite electrode, thereby forming a short circuit and causing safety problems. Therefore, it is imperative to find long-term materials with high safety, high energy, high performance and long life [2].

Lithium titanate ($\text{Li}_4\text{Ti}_5\text{O}_{12}$, LTO) is regarded as one of the most promising anode materials and can replace graphite materials [3]. LTO is a white powder possessing a spinel structure (Figure 1), and it has a high charge and discharge platform (approximately 1.5 V vs. Li/Li^+), which can effectively avoid the deposition of lithium dendrites on the electrode surface, thereby improving the safety of the battery [4]. In addition, the volume of the material is almost unchanged during charging and discharging, which makes a zero-strain material. Such a material normally has stable cycle performance and high stability, and can avoid structural damage caused by repeated shrinkage of the material [5].

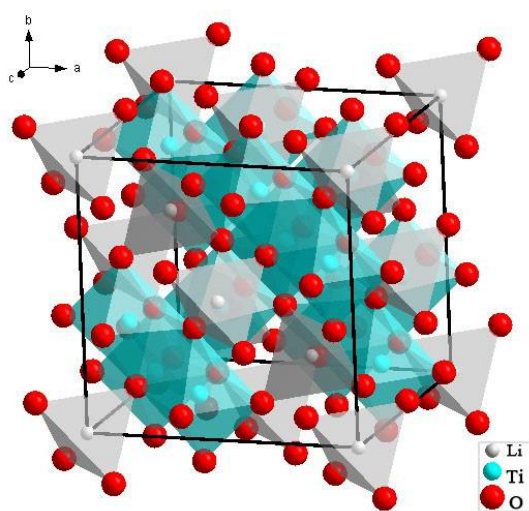


Figure 1. Schematic diagram of $\text{Li}_4\text{Ti}_5\text{O}_{12}$

However, LTO used as a lithium ion anode material has some shortcomings. LTO is a nearly insulating material, which results in its poor electrical conductivity due to the lack of electrons in the 3d electronic layer of Ti^{4+} . Its poor crystallinity also leads to a relatively low coulombic efficiency in the initial cycle of the charge/discharge process. During the battery cycle, the nanoparticles easily agglomerate, causing the battery capacity to decay quickly [6]. To improve the electrochemical performance of LTO, series of modification methods such as ion doping, morphology change and surface coating methods have been adopted.

To date, improving the conductivity and electrochemical performance of LTO can be achieved via ion doping which mainly replaces the positions of Li, Ti, and O in LTO with various elemental ions. In recent years, researchers have tried using different elements, such as Al [7], W [8], Co [9], Mn [10], Cu [11], Si [12], and Al [13]. The morphology change is mainly carried out by adding some nanomaterials, which can not only increase the lithium ion migration rate but also reduce the electrode

polarization and the capacity decay rate, thus finally enhancing the electrochemical performance and the stability of the material. Carbon, metal, and metal oxide surface coatings have also been applied without changing the structure of LTO to improve its conductivity as well as the diffusion rate of lithium ions [14-16].

Previous research shows that adding some metallic nanoparticles to the LTO nanoflakes can increase the electrical conductivity of the electrode, which greatly enhances the electrochemical performance of LTO [15]. With a high conductivity of $10^8 \text{ S}\cdot\text{cm}^{-1}$, Ag is considered to be a potential candidate for LTO. Erdas et al. [17] successfully synthesized LTO/Ag composite materials via a simple sol-gel method and used them as anode materials. The LTO/Ag composite material showed a significantly improved stability and rate capability, which exhibited a discharge capacity of $88 \text{ mAh}\cdot\text{g}^{-1}$ at 10 C. Krajewski et al. [18] designed and synthesized LTO/n-Ag nanoflakes by a three-step solid-state process. When the pristine material was modified with 1% Ag, the fabricated powders exhibited remarkably good cyclability, and the electrode showed high-rate performance. Its rate capacity was $100.13 \text{ mAh}\cdot\text{g}^{-1}$ at 10 C. Li et al. [19] successfully fabricated LTO/Ag through a two-step solid phase sintering process followed by subsequent electroless plating in the presence of silver. The first special discharge capacities reached $126.1 \text{ mAh}\cdot\text{g}^{-1}$ at 10 C. Note from the above limited literature that the synthesis process normally contains two sintering steps which may destroy the nanostructure of LTO and may have a negative effect on the electrochemical performance, especially the high-rate performance of the material.

In this research, a hydrothermal method followed by one-step calcination was used to synthesize Ag-modified LTO (designated Ag@LTO) nanoflakes used as LIB anodes. X-ray diffraction (XRD), scanning electron microscopy (SEM), transmission electron microscopy (TEM), and X-ray photoelectron spectroscopy (XPS) were applied to characterize the microstructures of LTO nanoflakes prepared with and without modification by Ag. The corresponding electrochemical performances were also studied by performing galvanostatic charge-discharge, cycle voltammetry (CV) and electrochemical impedance spectroscopy (EIS) tests to verify the influence of Ag on the LTO nanoflake electrode.

2. EXPERIMENTAL

2.1 Synthesis of LTO Flakes and Ag@ LTO Nanoflakes

Titanium (IV) butoxide (TBOT, AR, $\geq 98.5\%$, Titan Scientific Co., Ltd, Shanghai, China), lithium hydroxide monohydrate ($\text{LiOH}\cdot\text{H}_2\text{O}$, 99%, Titan Scientific Co., Ltd, Shanghai, China), and silver nitrate (AgNO_3 , AR, $\geq 99.8\%$, Titan Scientific Co., Ltd, Shanghai, China) were used to prepare LTO nanoflakes and Ag@LTO composites. $\text{LiOH}\cdot\text{H}_2\text{O}$ (0.21 g) and TBOT (1.7 mL) were first dissolved in ethanol with stirring for 16 h. Then, 25 mL deionized water was added to the mixed solution with a high stirring speed for 1 minute. Then, the milky white solution was placed in a 75 mL Teflon-lined stainless steel autoclave and heated at $180 \text{ }^\circ\text{C}$ for 36 h. The LTO precursors ($\text{Li}_{1.81}\text{H}_{0.19}\text{-Ti}_2\text{O}_5\cdot 2\text{H}_2\text{O}$) were finally obtained by filtering and drying at $80 \text{ }^\circ\text{C}$ overnight. Finally, white powders (LTO) were successfully synthesized by calcining in a muffle furnace at $600 \text{ }^\circ\text{C}$ for 6 h with a heating rate of $1 \text{ }^\circ\text{C}\cdot\text{min}^{-1}$.

For Ag@LTO composites, different amounts of AgNO₃ (3 wt.%, 5 wt.%, 7 wt.% and 9 wt.%) particles and LTO precursors were dissolved in 15 mL ethanol under stirring to form a black solution, and the received solution was dried at 80 °C for 10 h. The calcination conditions were kept the same of as those used for LTO. Finally, grey powders (Ag@LTO) with various Ag contents were obtained. The whole process used to prepare the samples is intuitively shown in Figure 2.

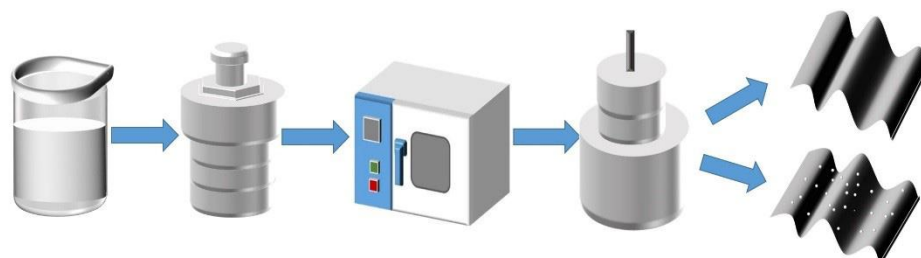


Figure 2. Schematic illustration of the hydrothermal process

2.2 Materials characterization

The crystal structures of the LTO and modified samples were investigated by X-ray diffraction (XRD, D2-PHASER, Bruker, Karlsruhe, Germany) with a scanning range of 5°-90° (with a rate of 1°/min) using a Cu-K α radiation source ($\lambda = 0.1540560$ nm). The morphologies and microstructures of the prepared samples were analyzed by a combination of field emission electron microscopy (FESEM, S-4800, HITACHI, Tokyo, Japan) equipped with energy dispersive spectroscopy (EDS, X-MAX 65T, OXFORD, England, UK) and transmission electron microscopy (TEM, JEM-2100F, JOEL, Tokyo, Japan). The chemical valence states of the synthesized samples were confirmed by X-ray photoelectron spectroscopy (XPS, ESCALAB250XI, Thermo Fisher Scientific, Waltham, MA, USA). A C 1s peak of the intrinsic carbon at 284.8 eV was used for charge correction. The XPS spectra were analyzed by XPSPEAK software.

2.3 Electrode preparation

The electrochemical tests were evaluated with 2032 coin cells using lithium metal foil as the opposite electrode. The active material (Li₄Ti₅O₁₂ or Ag@LTO nanoflakes), binder (PVDF) and carbon source (acetylene black) were mixed with a mass ratio of 8:1:1 in a high-speed vibrating ball milling machine (MSK-SFM-12M, HF-Kejing, China). A small amount of N-methyl-2-pyrrolidone (NMP) was then added to the mixture and stirred to form a slurry. A Cu foil with a diameter of 16 mm was coated with slurry and dried at 60 °C overnight. Finally, the working electrode was successfully obtained. Celgard 2300 polypropylene was used as the separator, and the electrolyte was prepared by dissolving 1 M LiPF₆ in a mixture of ethylene carbonate (EC) and diethyl carbonate (DEC) with a volume ratio of 1:1. The 2032 coin cells were finally assembled in a glove box (Super 1220/750/900, Shanghai Mikrouna Electromechanical Technology Co., Ltd, Shanghai, China) with built-in high-purity argon gas (99.999%

purity). The water and oxygen levels of the glove box were maintained below 1 ppm before the battery was assembled.

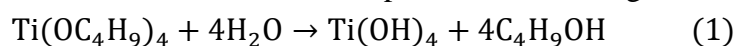
2.4 Electrochemical measurements

The electrochemical properties of the 2032 button batteries were examined with an electrochemical workstation (CT 4008, Neware Electronics Co., Ltd, China). The cycle stability was evaluated by performing charge-discharge tests at 1-3 V and $32 \text{ mA}\cdot\text{g}^{-1}$ for 100 cycles. The rate performance was evaluated at different current densities (32, 80, 160, 480, 800 and $1600 \text{ mA}\cdot\text{g}^{-1}$). Cyclic voltammetry (CV) was performed on an electrochemical workstation (CHI 760E, CH Instruments Ins, China). The scan rate ranged from 1-3 V at $0.1 \text{ mV}\cdot\text{s}^{-1}$. Electrochemical impedance spectroscopy (EIS) was carried out with an electrochemical workstation (CS 310H, China) with the frequencies ranging from 0.1 MHz to 0.01 Hz and the AC voltage amplitude was set to 5 mV. All electrochemical performances were tested at room temperature.

3. RESULTS AND DISCUSSION

3.1 Phase and Morphology Characterization of the LTO and Ag@LTO samples

XRD patterns of the pristine LTO and Ag-modified samples are given in Figure 3. All diffraction peaks are narrow and sharp, indicating that the samples have good crystallinity. The indexed results indicate that the XRD patterns of the pristine sample are in good agreement with the XRD pattern of standard LTO with a spinel structure (JCPDS, NO.49-3722). The synthesis of LTO can be clearly described by Reactions (1)-(3). $\text{Ti}(\text{OC}_4\text{H}_9)_4$ with activity first reacted with H_2O , resulting in the formation of $\text{Ti}(\text{OH})_4$. Metastable $\text{Ti}(\text{OH})_4$ subsequently decomposed into TiO_2 and H_2O . Then TiO_2 reacted with LiOH at high temperature and high pressure to produce Li-Ti-O precursor. The precursor that was subjected to the high-temperature treatment finally transformed into pristine LTO [20]. When 3 wt.% Ag was introduced into pristine LTO, four new weak diffraction peaks appeared at 38.1° , 44.3° , 64.5° , and 77.4° , which confirmed the existence of metallic silver (JCPDS, No. 01-089-8428). The existence of Ag is mainly attributed to the thermal decomposition of AgNO_3 at an atmospheric temperature of approximately 444°C [21]. This implies that Ag@LTO composites were successfully synthesized. The intensities of the peaks related to Ag increased as the content of Ag increased to 3 wt.%, 5 wt.%, 7 wt.% and finally 9 wt.%, indicating that the volume fraction of metallic silver in the samples increased correspondingly. The diffraction peaks associated with LTO have almost no shift with the increase in Ag content to 7 wt.%, implying that the added Ag does not enter the lattice of the pristine LTO, and mainly exists in the form of metallic silver. However, the strongest characteristic peak of LTO (111) slightly moves towards the left when the added amount of Ag is increased to 9 wt. %, as shown in Figure 4, which may result from a substitutional compound of $\text{Li}_4\text{Ti}_{5-x}\text{Ag}_x\text{O}_{12}$ [22].



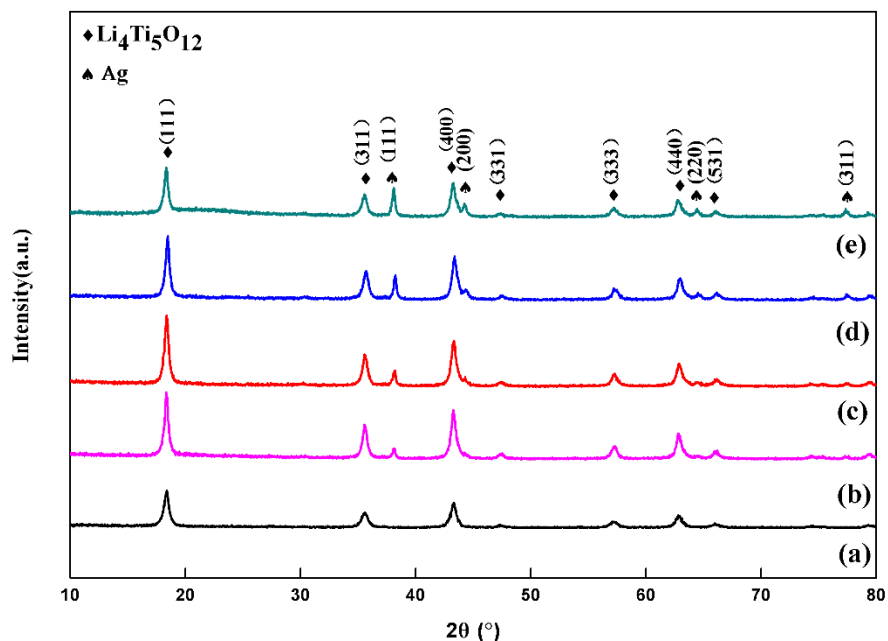


Figure 3. XRD patterns of (a) pristine LTO, (b) 3 wt.% Ag@LTO, (c) 5 wt.% Ag@LTO, (d) 7 wt.% Ag@LTO, and (e) 9 wt.% Ag@LTO

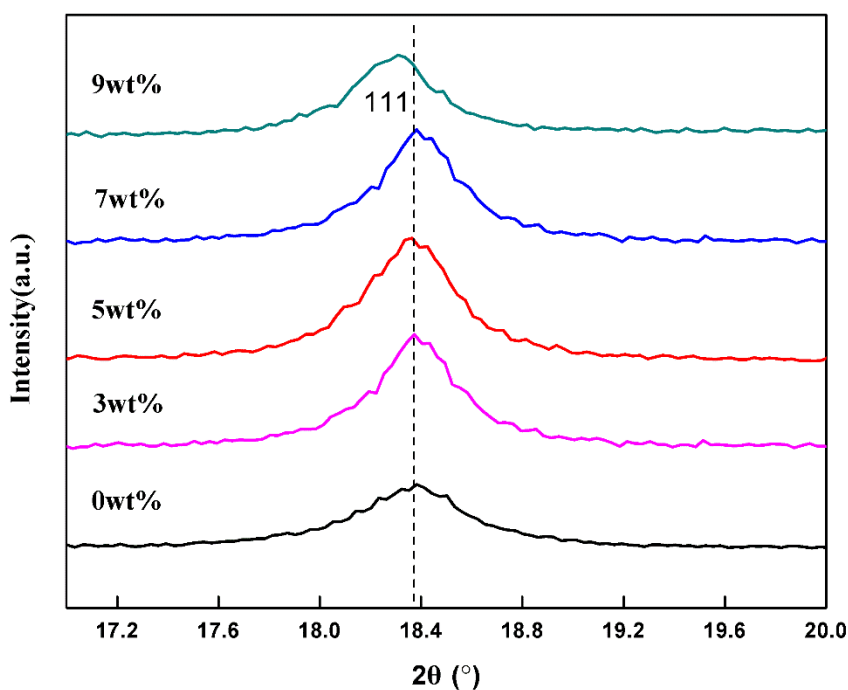


Figure 4. Enlarged (111) peak of Ag@LTO

The SEM morphologies of LTO and 7 wt.% Ag@LTO are shown in Figure 5. The two samples are composed of numerous flake-like particles of different sizes, which cluster together and grow into

the comparatively coarse flower-like particles. Comparatively speaking, the LTO particles become finer after Ag addition, which indicates that the existence of Ag may inhibit the growth of LTO grains. The SEM image at higher magnification reveals that the surface of pristine LTO particles is comparatively smooth, however some fine spherical particles (~53 nm in average diameter) adhere to the surface of LTO particles resulting from the addition of Ag. EDS mapping and scanning was employed to identify the distribution of Ti, O and Ag in the particles. As shown in Figure 5 (e-h), the particles are rich in Ti and O. Ag is uniformly distributed in the particles, however, its content is far lower than that of Ti and O. Moreover, it can be observed that the content of Ag in the dispersedly distributed spherical particles is higher than that in the other zones. This implies that fine Ag particles may be distributed in both the inner and the outer parts of the LTO particles.

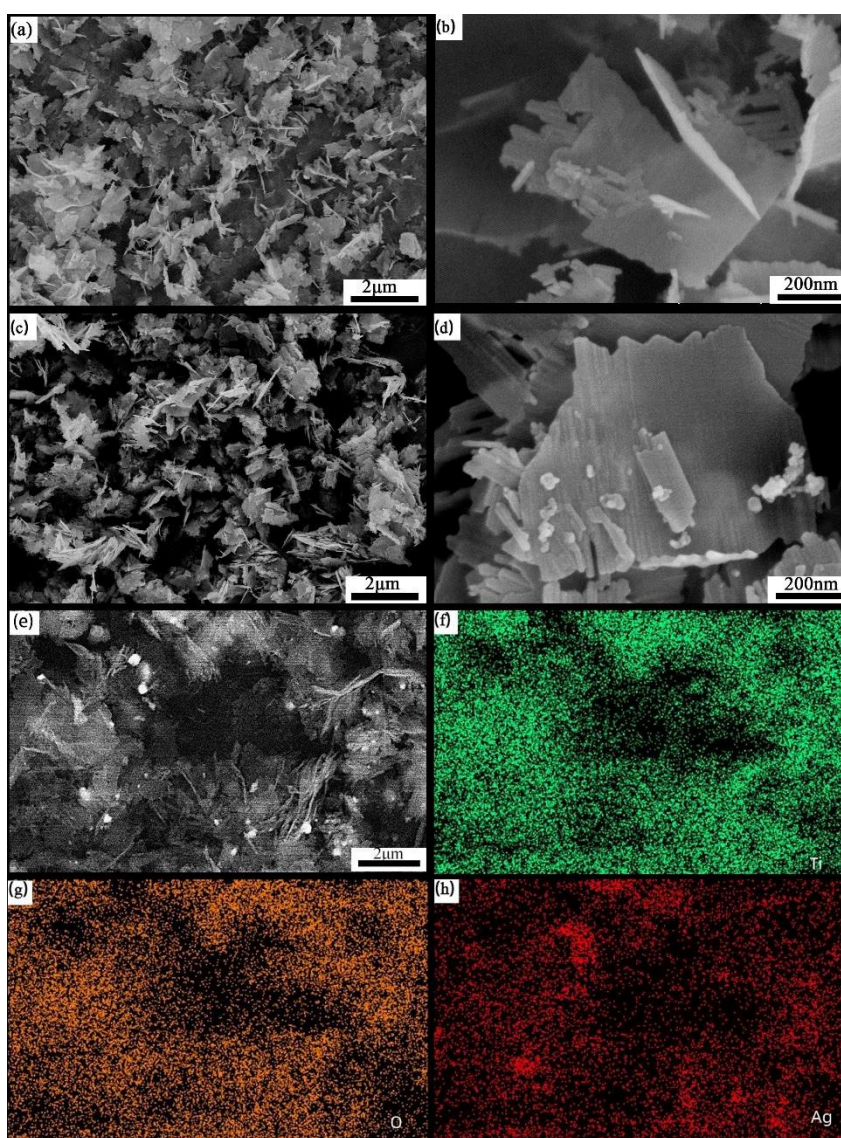


Figure 5. FE-SEM images of (a, b) LTO nanoflakes and (c, d) Ag@LTO nanoflakes. (e-h) SEM image of Ag@LTO and corresponding EDS mapping image of Li, Ti and O.

Figure 6(a) shows the corresponding TEM images of Ag@LTO. The surface of LTO is covered by irregular Ag particles with an average size of 50 nm, which is in accordance with the SEM results. Figure 6(b) shows the HRTEM image of Ag@LTO, from which the measured interplanar spaces of the pristine LTO (111) crystal plane and the Ag (111) crystal plane are 0.4804 nm and 0.2352 nm, respectively. This further proves that Ag exists in the form of metallic particles. Selected area electron diffraction (SAED) was also performed on the Ag@LTO composite. Ring patterns can be found in Figure 6(c) indicating a polycrystalline structure. Calculating the d value and comparing with the JCPDS card, show that the LTO and Ag in the composite sample are polycrystalline.

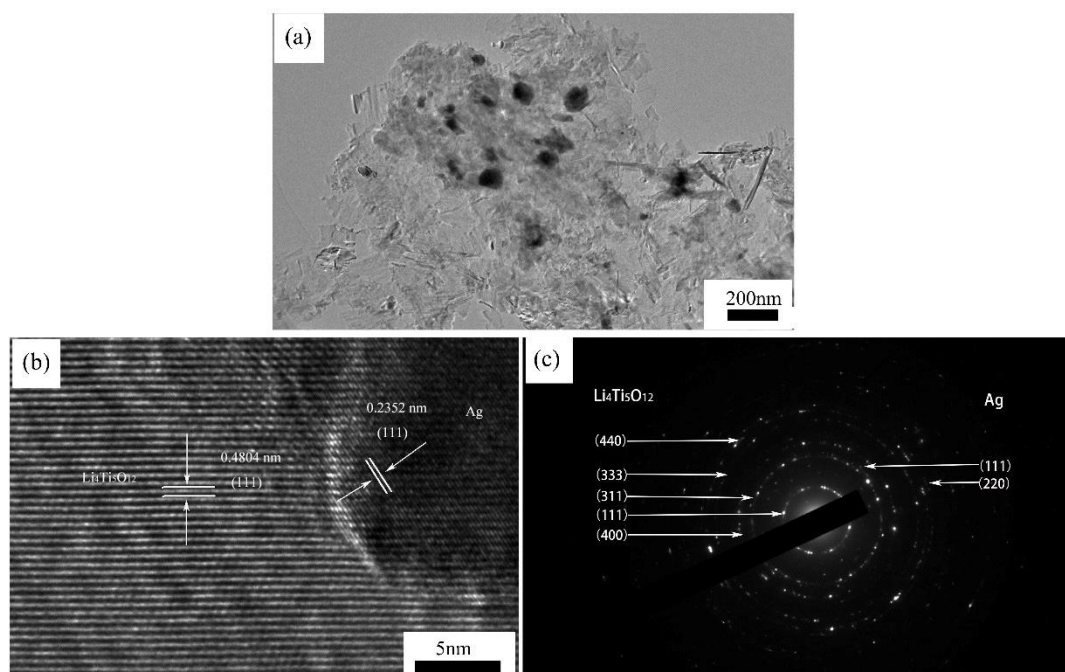


Figure 6. (a) TEM images of Ag@LTO nanoflakes. (b) HRTEM image of a section of an Ag@LTO nanoflake. (c) SAED patterns of an Ag@LTO nanoflake

XPS analysis was carried out to obtain more evidence of the valence states of Ti and Ag in the Ag@LTO composite materials. Figure 7(a) presents the XPS survey spectrum of the Ag@LTO composite with 7 wt. % Ag. Li, Ti and O are the main elements involved in the sample. Trace amounts of C are also detected, which may be ascribed to the carbon contaminants from the instrument or the preparation of the samples [23]. A peak with a binding energy of 54.58 eV can be clearly observed in the high resolution spectrum of Li 1s (Figure 7(b)), which results from the Li-O bond. The Ti 2p spectrum is composed of two peaks, corresponding to Ti 2p_{3/2} at 458.46 eV and Ti 2p_{1/2} at 464.23 eV (Figure 7(c)), which confirms the existence of Ti⁴⁺. Two O1s peaks at 529.84 eV and 531.77 eV (Figure 7(d)) are associated with lattice oxygen in LTO and the absorbed oxygen on LTO surfaces [18]. The high resolution spectrum of Ag 3d consists of two individual peaks at 367.65 eV and 373.61 eV (Figure 7(e)),

which suggest the existence of metallic silver. XPS further confirmed that LTO was synthesized, and metallic silver was successfully introduced into LTO.

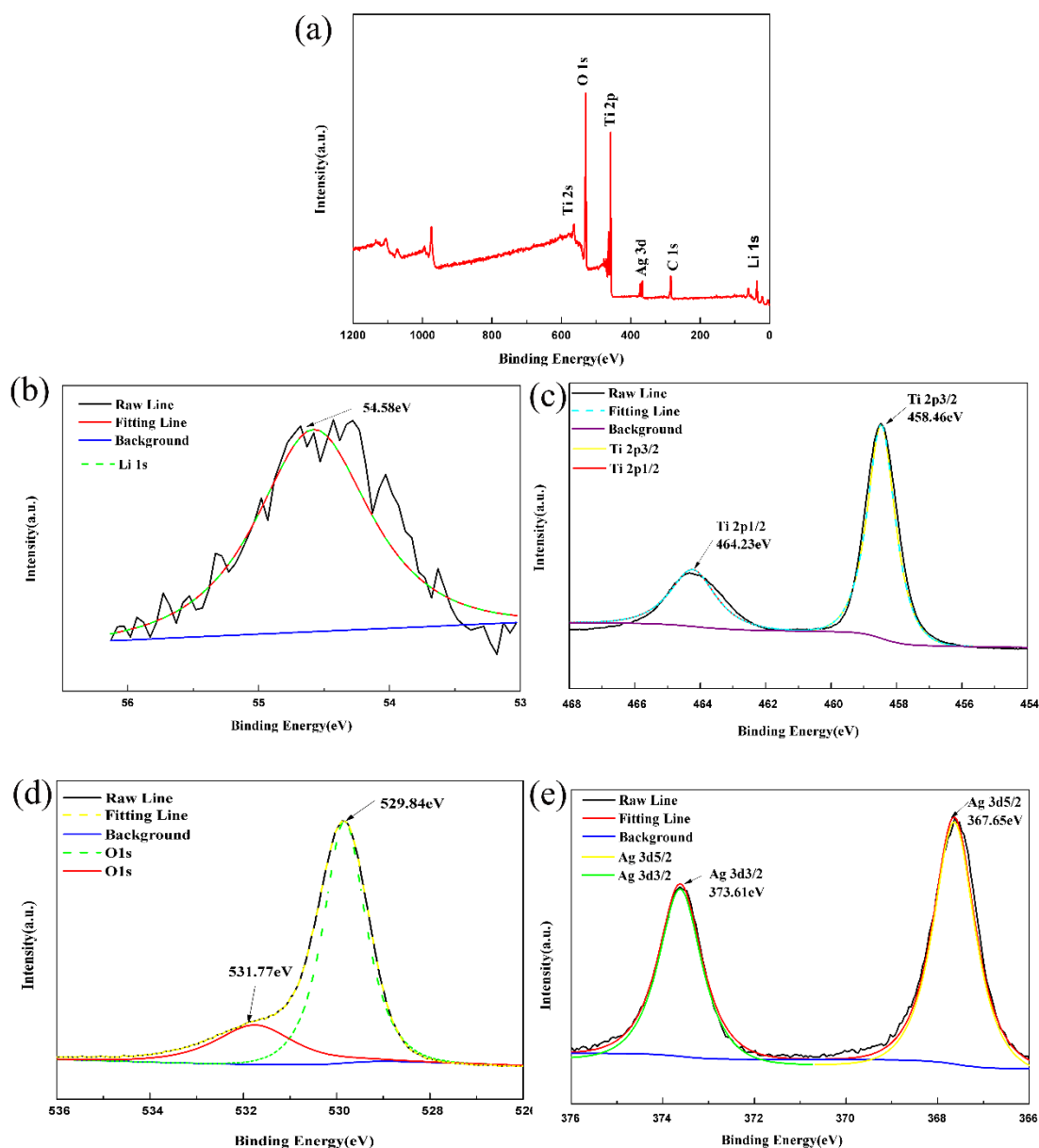


Figure 7. (a) XPS survey spectra of the Ag@LTO nanoflakes; high-resolution Li 1s (b) Ti 2p (c), O 1s (d) and Ag 3d (e) XPS spectra of the Ag@LTO nanoflakes.

3.2 Electrochemical Performances of the LTO and Ag@LTO samples

Figure 8(a) shows the first charge/discharge curves of the pristine LTO and Ag@LTO composites at $32 \text{ mA}\cdot\text{g}^{-1}$. Compared with the unmodified LTO, it is clear that the specific discharge capacity of LTO presents an upward tendency for Ag amounts ranging from 0 to 7 wt.% (160.35, 211.79, 222.32, and $256.75 \text{ mAh}\cdot\text{g}^{-1}$). Nevertheless, the specific discharge capacity decreased as more Ag was introduced

into LTO (9 wt.%). This is probably due to the formation of a substitutional compound of $\text{Li}_4\text{Ti}_5\text{-xAg}_x\text{O}_{12}$, in which the spinel structure of LTO may be destroyed by Ag^+ due to its relatively large radius. During the second and third charge/discharge cycles (Figure 8(b-c)), the specific discharge capacity of the samples illustrates a similar tendency. The coulombic efficiency of the pristine LTO is 83.54% in the first cycle, and in the third cycle, it retains approximately 93.23% of its coulombic efficiency with a specific discharge capacity of $143.71 \text{ mAh}\cdot\text{g}^{-1}$. When 7 wt.% Ag was introduced into the pristine LTO, the coulombic efficiency of the Ag@LTO electrode reached 66.66% in the first cycle, while in the third cycle, it retained approximately 94.68% of its coulombic efficiency with a relatively high specific discharge capacity of $157.25 \text{ mAh}\cdot\text{g}^{-1}$. The initial low coulombic efficiency may be related to electrolyte decomposition during the initial discharge process and the effect of the formation of the SEI layer. The increase in discharge capacity is attributed to the addition of Ag which accelerates the transportation of electrons. The optimal amount of added Ag can be confirmed as 7 wt.%, and this sample exhibits the highest specific discharge capacity.

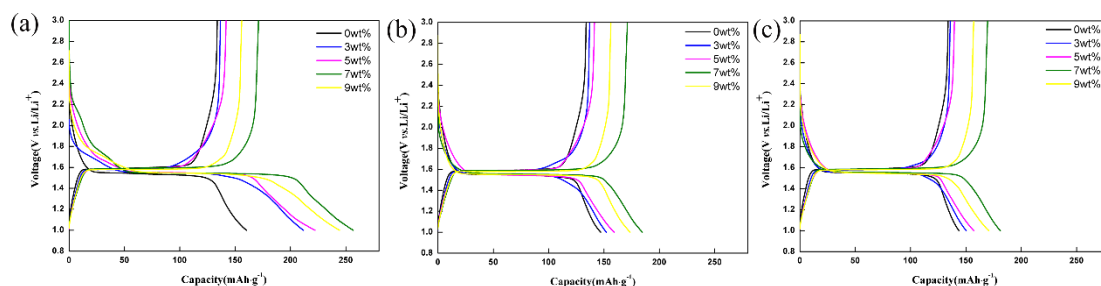
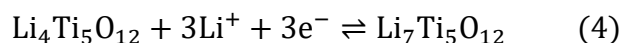


Figure 8. (a-c) The first-third discharge/charge curves of $\text{Li}_4\text{Ti}_5\text{O}_{12}$ and Ag@ $\text{Li}_4\text{Ti}_5\text{O}_{12}$ composites with different silver ratios.

Figure 9(a,b) illustrates the CV curves of the pristine LTO and Ag@LTO nanoflake anodes for the first cycle to the third cycle in a voltage range of 1-2.5 V (vs Li^+/Li) with a scanning rate of 0.1 mV/s. Similar redox peaks can be found for both the LTO and Ag-modified samples, which result from Li^+ intercalation and deintercalation in LTO and can be described by the following intercalation and deintercalation reaction:



Note in Figure 9(a) and Figure 9(b) that these redox peaks overlap during the first cycle to the third cycle, implying a high coulombic efficiency for both pristine LTO and Ag@LTO. For Ag@LTO, the curve shows that the potential of the oxidation peak is 1.65 V, corresponding to a charge process in which Li^+ deintercalates, and the potential of the reduction peak is 1.52 V corresponding to a discharge process in which Li^+ intercalates. The potential difference between these two peaks for Ag@LTO is 0.13 V, which is smaller than that for the pristine LTO (0.14 V), indicating that Ag reduced the electrode polarization. Meanwhile, the CV area of the Ag@LTO composite is larger than that of LTO, implying that Ag@LTO possesses a higher specific capacity. Therefore, it can be concluded that Ag particles not

only reduced the electrode polarization but also increased the diffusion rate of Li^+ , thereby increasing the capacity of pristine LTO.

The specific charge/discharge curves obtained by cycling LTO and Ag@LTO for one hundred cycles at a current density of $32 \text{ mA}\cdot\text{g}^{-1}$ are illustrated in Figure 9(c) and Figure 9(d). Ag@LTO (Figure 9(d)) exhibits initial first and second discharge capacities of $256.67 \text{ mAh}\cdot\text{g}^{-1}$ and $175.86 \text{ mAh}\cdot\text{g}^{-1}$, respectively, obtaining a capacity retention rate of 68.52%. The initial capacity loss may be related to electrolyte decomposition in the initial discharge process and the effect of the formed SEI layer [24]. Because the formation process of the SEI layer will consume large number of lithium ions during lithium ion insertion, the number of lithium ions will be fixed in the SEI layer, leading to a lower capacity retention rate. After that, the SEI layer will reach a steady state and the number of insertions and deinsertions of lithium ions will gradually increase during the following charge/discharge process. Finally, the coulombic efficiency is gradually increased. The higher specific capacity of Ag@LTO than that of LTO is probably due to the added Ag particles, which significantly influenced the absorbed number of lithium ions in LTO, increased the migration rate of lithium ions and reduced the migration path of lithium ions [25].

Figure 9(e) shows the cycling stability of pristine LTO and Ag@LTO up to 100 cycles. The coulombic efficiency of the pristine LTO is 98.03% for the 25th cycle, and this value finally remains at approximately 98.92% with a specific discharge capacity of $126.64 \text{ mAh}\cdot\text{g}^{-1}$. The relatively stable cycle stability of pristine LTO is because lithium ion intercalation and deintercalation in the cycling process of LTO always maintain their own unique zero strain capacity [26]. After adding an appropriate Ag amount to the LTO, the coulombic efficiency of the Ag@LTO anode reaches 98.35% after the 25th cycle, and this value finally increases to ~99.47% with a relatively high specific discharge capacity of $146.97 \text{ mAh}\cdot\text{g}^{-1}$ after one hundred cycles. The charge and discharge capacity of the Ag@LTO composite is higher than that of pristine LTO, which may be related to lithium ion intercalation and deintercalation. Therefore, the addition of Ag enhances both the conductivity and the insertion/deinsertion ability of lithium ions in LTO, resulting in the improvement of the charge-discharge specific capacity and cycle performance of the material.

Figure 9(f) mainly presents the rate performances of $\text{Li}_4\text{Ti}_5\text{O}_{12}$ and Ag@LTO at different current densities. The current densities used are 32, 80, 160, 480, 800 and $1600 \text{ mA}\cdot\text{g}^{-1}$. The average specific discharge capacity of pristine LTO decreased from $154.36 \text{ mAh}\cdot\text{g}^{-1}$ to $102.91 \text{ mAh}\cdot\text{g}^{-1}$, corresponding to a retention rate of 66.67%. When the applied current density returned to the initial $32 \text{ mA}\cdot\text{g}^{-1}$ value, 91.02% of its capacity value was retained ($140.5 \text{ mAh}\cdot\text{g}^{-1}$). In contrast, the average specific discharge capacity of Ag@LTO decreased from $181.15 \text{ mAh}\cdot\text{g}^{-1}$ to $146.56 \text{ mAh}\cdot\text{g}^{-1}$, corresponding to relatively higher retention rate of 80.91%. When the applied current density returned to the initial value, 93.04% of its initial capacity was retained ($168.55 \text{ mAh}\cdot\text{g}^{-1}$), indicating that the addition of Ag increased the rate performance of pure LTO.

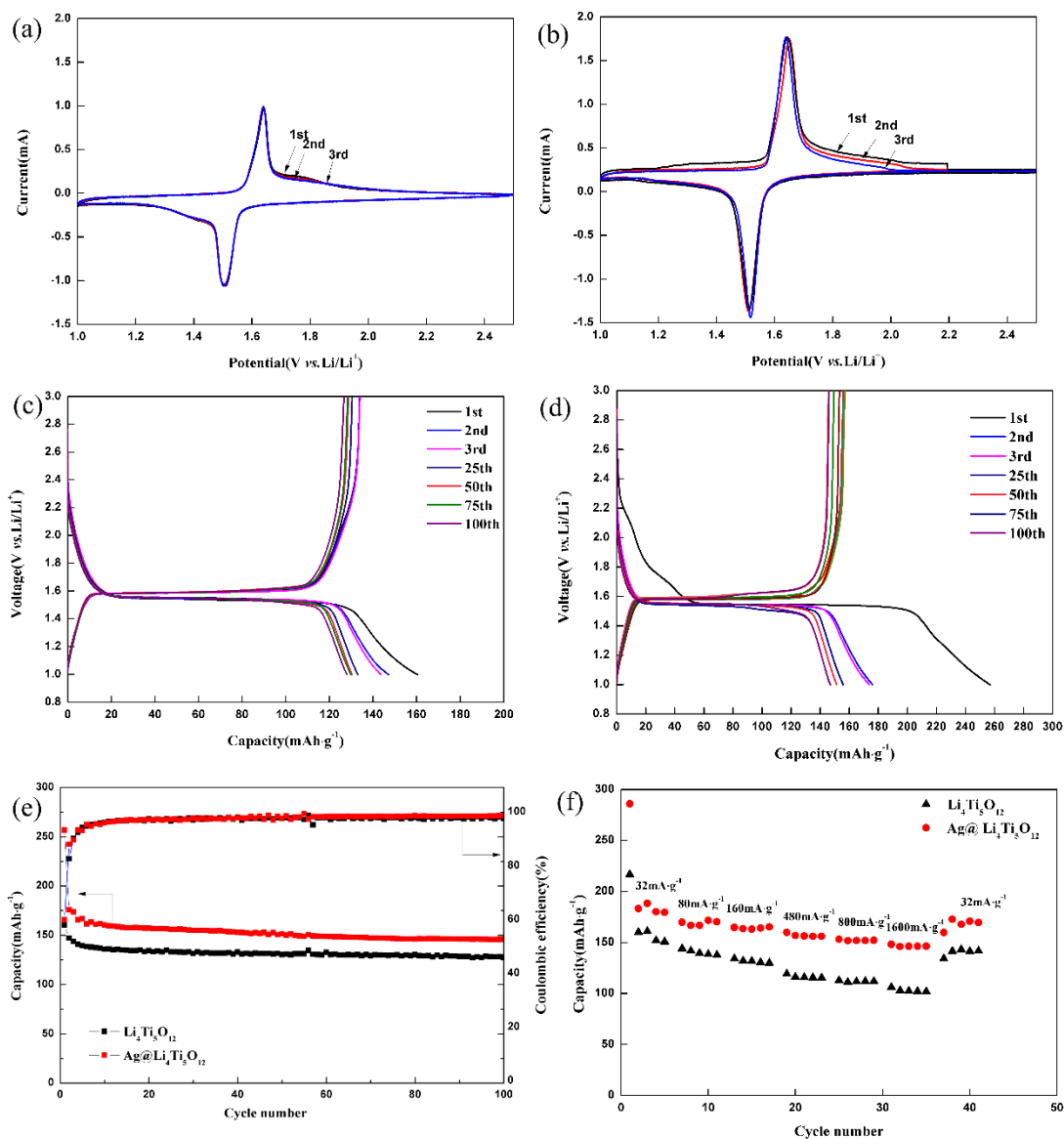


Figure 9. Electrochemical performances of LTO and Ag@LTO nanoflake electrodes. Cyclic voltammograms of: (a) LTO nanoflakes and (b) 7 wt.% Ag@LTO nanoflakes for the initial first cycle to the third cycle with a scanning rate of 0.1 mV/s for cycling between 1 and -3 V; (c) discharge curves of the LTO nanoflake electrode and (d) 7 wt.% Ag@LTO nanoflake electrode obtained by cycling 100 cycles times at 32 mA·g⁻¹; (e) cycling performance of LTO and Ag@LTO nanoflakes at 32 mA·g⁻¹ and (f) rate capability of LTO and Ag@LTO nanoflake electrodes at different current densities.

The electrochemical performance of the Ag@LTO nanoflakes obtained in our research is also compared with that of Li₄Ti₅O₁₂ composites reported in other references [27-33]. As shown in Table 1, the Ag@LTO composite prepared in this work exhibits excellent electrochemical properties. The specific discharge capacity is 176.80 mAh·g⁻¹ at 32 mA·g⁻¹, and when the modified electrode is subjected to 100 cycles at 32 mA·g⁻¹, its specific discharge capacity is still retained at a relatively high value of 146.97 mAh·g⁻¹. Note that when the Ag@LTO nanoflake electrode undergoes discharge/charge

processes at various current densities (32 mA·g⁻¹, 80 mA·g⁻¹, 160 mA·g⁻¹, 480 mA·g⁻¹, 800 mA·g⁻¹, 1600 mA·g⁻¹), it can still exhibit an excellent rate capability with a higher discharge capacity of 146.56 mAh·g⁻¹, which is superior to the discharge capacity of the reported references. Therefore, the electrochemical performances, especially the rate capability of the Ag@LTO nanoflake electrode prepared in this study are comparable to those in the literature.

Table 1. Comparison of some electrochemical performances for LTO composites reported in previous works

Ref.	Materials	Initial discharge capacity	Cycle performance	Rate performance
This work	Ag@LTO nanoflakes	176.80 mAh·g ⁻¹ at 32 mA·g ⁻¹	146.97 mAh·g ⁻¹ / 100 cycles at 32 mA·g ⁻¹	146.56 mAh·g ⁻¹ /1600 mA·g ⁻¹
[27]	CuO@LTO nanoflakes	160 mAh·g ⁻¹ at 100 mA·g ⁻¹	169.6 mAh·g ⁻¹ / 10 cycles at 160 mA·g ⁻¹	38 mAh·g ⁻¹ /1000 mA·g ⁻¹
[28]	C/LTO/rGO nanoflakes	159.8 mAh·g ⁻¹ at 16 mA·g ⁻¹	150 mAh·g ⁻¹ / 200 cycles at 33 mA·g ⁻¹	80 mAh·g ⁻¹ /1500 mA·g ⁻¹
[29]	TiO ₂ @LTO nanoflakes	125 mAh·g ⁻¹ at 68.5 mA·g ⁻¹	60 mAh·g ⁻¹ / 150 cycles at 100 mA·g ⁻¹	100 mAh·g ⁻¹ /960 mA·g ⁻¹
[30]	rGO @LTO nanoflakes	120 mAh·g ⁻¹ at 160 mA·g ⁻¹	52 mAh·g ⁻¹ / 150 cycles at 160 mA·g ⁻¹	105 mAh·g ⁻¹ /3200 mA·g ⁻¹
[31]	Carbon cloth@LTO nanoflakes	118 mAh·g ⁻¹ at 1000 mA·g ⁻¹	150 mAh·g ⁻¹ / 250 cycles at 200 mA·g ⁻¹	100 mAh·g ⁻¹ /1000 mA·g ⁻¹
[32]	LTO/C/Ag nanoflakes	175 mAh·g ⁻¹ at 20 mA·g ⁻¹	178 mAh·g ⁻¹ / 35 cycles at 20 mA·g ⁻¹	62 mAh·g ⁻¹ /800 mA·g ⁻¹
[33]	LTO/Ag nanoflakes	178.72 mAh·g ⁻¹ at 0.1 C	172.21 mAh·g ⁻¹ / 100 cycles at 0.2 C	155 mAh·g ⁻¹ /5 C

To fully understand the electrochemical mechanism, EIS curves of LTO (Ag@LTO) were obtained to prepare Nyquist plots as shown in Figure 10. An EIS curve is generally composed of two parts: a semicircle formed in high-and intermediate-frequency regions and a slash in the low-frequency region. The intercept formed in front of the intersection of the semicircle and the real part of the impedance is the internal resistance of the battery (solution resistance) corresponding to R_s in the equivalent circuit, which mainly comes from the interaction between the electrode sheet and the electrolyte. The diameter of the semicircle corresponding to the charge transfer resistance (R_{ct}) is mainly related to the complex electrochemical reaction between the interface of the electrode and the electrolyte. The larger the diameter of the semicircle is, the greater the charge transfer resistance of the electrode material will be. CPE represents passivation film capacitance and double-layer capacitance. Warburg impedance is mainly related to lithium ion diffusion (W). The characteristic is that the greater the slope of the diagonal is, the smaller the impedance will be. The introduction of Ag results in a decrease in R_{ct} from 302.29 Ω to 178.56 Ω after addition. Moreover, the increase in the slope of the straight line proves that the diffusion resistance of Li^+ into the electrode is clearly reduced because of the addition of Ag.

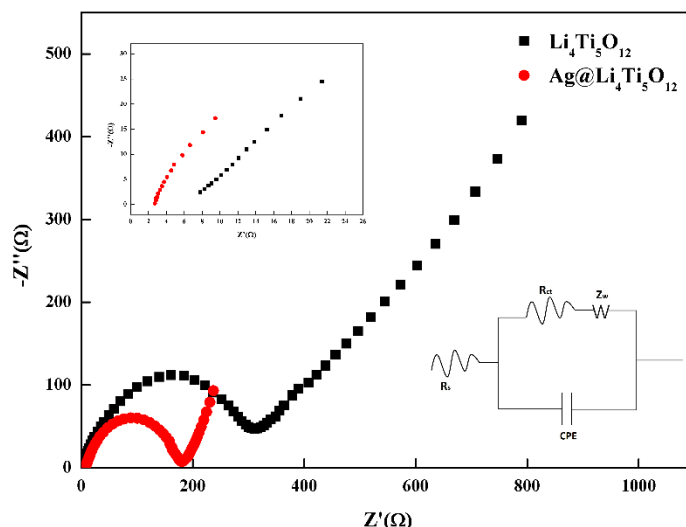


Figure 10. Nyquist plots of the pristine LTO nanoflake electrode and Ag@LTO nanoflake electrode at room temperature.

Figure 11 shows the connection between the plot of Z_{re} and the reciprocal square root of the lower angular frequencies. The straight line is mainly due to the diffusion of lithium ions in the electrode material, and the slope is the Warburg impedance coefficient (σ_w). The coefficients of lithium ion diffusion into the electrode material (D_{Li}) can be calculated by Eqs. (5)-(6), and are recorded in Table 2.

$$D_{Li} = \frac{R^2}{2A^2n^4F^4C_{Li}^2\sigma_w^2} \quad (5)$$

$$Z_{re} = R_s + R_{ct} + \sigma_w \cdot \omega^{-\frac{1}{2}} \quad (6)$$

in which ω is the angular frequency ($\text{rad}\cdot\text{s}^{-1}$), R is the gas constant ($8.314 \text{ J}\cdot\text{mol}^{-1}\cdot\text{K}^{-1}$), F is Faraday’s constant ($96500 \text{ C}\cdot\text{mol}^{-1}$), T is the absolute temperature (K), D_{Li} is the lithium ion diffusion coefficient ($\text{cm}^2\cdot\text{s}^{-1}$), C_{Li} is the concentration of lithium ions ($\text{mol}\cdot\text{cm}^{-3}$), and σ_w is the Warburg coefficient, which can be obtained from the slope shown in Figure 11.

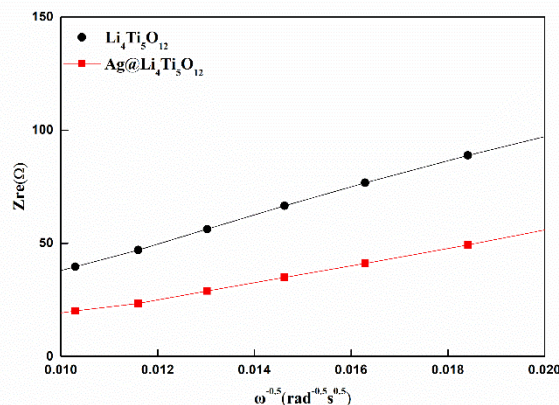


Figure 11. The relationship between Z_{re} and $\omega^{-0.5}$ at low frequencies.

Obviously, the diffusion coefficient D_{Li} of pristine $Li_4Ti_5O_{12}$ lithium ions increases significantly from $5.98 \times 10^{-11} \text{ cm}^2 \cdot \text{s}^{-1}$ to $4.77 \times 10^{-10} \text{ cm}^2 \cdot \text{s}^{-1}$, i.e., an increase of approximately an order of magnitude. The addition of Ag is beneficial to enhance the intercalation/deintercalation of Li^+ and improve the lithium ion diffusion coefficient.

Table 2. Impedance parameters of LTO and Ag@LTO composites

Samples	R_s/Ω	R_{ct}/Ω	$D_{Li}/\text{cm}^2 \cdot \text{s}^{-1}$
LTO	7.73	302.29	5.98×10^{-11}
Ag@LTO	2.67	178.56	4.77×10^{-10}

4. CONCLUSIONS

Ag@ $Li_4Ti_5O_{12}$ composites with different Ag amounts were successfully prepared by a hydrothermal method and subsequent one-step calcination. In summary, Ag nanoparticles with an average size of 53.33 nm are uniformly coated on the surface of $Li_4Ti_5O_{12}$. All the Ag@ $Li_4Ti_5O_{12}$ composites exhibit a higher charge-discharge specific capacity than pristine $Li_4Ti_5O_{12}$. The 7 wt.% Ag@ $Li_4Ti_5O_{12}$ composite shows the highest specific capacity of $256.75 \text{ mAh} \cdot \text{g}^{-1}$ and a coulombic efficiency close to 100% even after 100 cycles of discharging at $32 \text{ mA} \cdot \text{g}^{-1}$. This material also shows excellent rate capacity ($146.56 \text{ mAh} \cdot \text{g}^{-1}$) at a current density of $1600 \text{ mA} \cdot \text{g}^{-1}$. The improvement in electrochemical performance is mainly attributed to the addition of Ag, which enhances the conductivity of the material. The conductivity of $Li_4Ti_5O_{12}$ increases from $6.399 \times 10^{-6} \text{ S} \cdot \text{cm}^{-1}$ to $1.833 \times 10^{-5} \text{ S} \cdot \text{cm}^{-1}$ while its lithium ion diffusion coefficient increases from $5.982 \times 10^{-11} \text{ cm}^2 \cdot \text{s}^{-1}$ to $4.766 \times 10^{-10} \text{ cm}^2 \cdot \text{s}^{-1}$ after 7 wt.% Ag addition. The high reversible capacity, high rate capability and high cycle stability make Ag@ $Li_4Ti_5O_{12}$ a promising candidate LIB anode material.

ACKNOWLEDGMENTS

This work was financially supported by the National Natural Science Foundation of China, China (no. 51471105) and Natural Science Foundation of Shanghai (20ZR1422200).

DECLARATION OF INTEREST

None

References

1. K. Zhu, H. Gao, G. Hu, M. Liu, and H. Wang, *Power Sources*, 340 (2017) 263.
2. L. Shen, E. Uchaker, X. Zhang, and G. Cao, *Adv. Mater.*, 24 (2012) 6502.
3. T. Yuan, Z. Tan, C. Ma, J. Yang, Z. F. Ma, and S. Zheng, *Adv. Energy. Mater.*, 7 (2017) 1601625.
4. N. Y. Yao, H. K. Liu, X. Liang, Y. Sun, X. Y. Feng, C. H. Chen, and H. F. Xiang, *J. Alloy. Compd.*, 771 (2019) 755.

5. Y. Liu, X. Yan, B. Xu, J. Lan, Y. Yu, Yang X, Lin Y, and C. Nan, *Chem. Eng. J.*, 361 (2019) 1371.
6. R. Wen, J. Yue, Z. Ma, W. Chen, X. Jiang, and A. Yu, *Chinese Sci Bull.*, 59 (2014) 2162.
7. I. Nuroniah, S. Priyono, A. Subhan, B. Prihandoko, A. Suhandi, and Sohib A, *Mater. Today.*, 13 (2019) 65.
8. Z. Pu, Q. Lan, Y. Li, S. Liu, D. Yu, and X. J. Lv, *J. Power Sources.*, 437 (2019) 226890.
9. D. Wang, H. Liu, Z. Shan, D. Xia, R. Na, H. Liu, B. Wang, and J. Tian, *Energy Storage Mater.*, 27 (2020) 387.
10. S. Zou, G. Wang, Y. Zhang, C. Xue, H. Chen, G. Yang, H. Nan, H. Wei, and H. Lin, *J. Alloy Compd.*, 816 (2020) 152609.
11. X. Zhu, S. Zhou, X. Jiang, X. Yao, X. Xu, A. Peng, L. Wang, and Q. Xue, *J. Alloy Compd.*, 830 (2020) 154682.
12. M. Liu, H. Gao, G. Hu, K. Zhu, and H. Huang, *J. Energy Chem.*, 40 (2020) 89.
13. H. Zhao, Y. Li, Z. Zhu, J. Lin, and R. Wang, *Electrochim. Acta.*, 53 (2008) 7079.
14. D. Mu, Y. Chen, B. Wu, R. Huang, Y. Jiang, L. Li, and F. Wu, *J. Alloy. Compd.*, 671 (2016) 157.
15. J. Wang, F. Zhao, J. Chao, Y. Liu, and B. Wang, *Ionics*, 21 (2015) 2155.
16. M. Guo, S. Wang, L. X. Ding, C. Huang, and H. Wang, *J. Power Sources*, 283 (2015) 372.
17. A. Erdas, S. Ozcan, D. Nalci, M. O. Guler, and H. Akbulut, *Surf, Coat. Tech.*, 271 (2015) 136.
18. M. Krajewski, M. Michalska, B. Hamankiewicz, D. Ziolkowska, K. P. Korona, J. B. Jasinski, M. Kaminska, L. Lipinska, and A. Czerwinski, *J. Power Sources.*, 245 (2014) 764.
19. J. Li, S. Huang, S. Li, S. Xu, and C. Pan, *Ceram. Int.*, 43 (2017) 1650.
20. W. Liu, W. Tan, Y. Bai, Y. Wang, and X. Jia, *J. Chinese Ceram. Soc.*, 39 (2011) 1622.
21. S. Li, H. Zhang, K. Zhang, W. Sun, Y. Z. Wang, J. T. Chen, D. L. Tao, *Spectrosc Spect Anal.*, 31 (2014) 38.
22. Y. Zhu, T. Yi, H. Ma, Y. Ma, L. Jiang, R. Zhu, *J. Chem. Sci.*, 126 (2014) 17.
23. H. Hou, M. Shang, F. Gao, L. Wang, Liu Q, J. Zheng, Z. Yang, and W. Yang, *Acs. Appl. Mater. Inter.*, 8 (2016) 20128.
24. Y. Feng, H. Liu, X. Zhao, and W. Dong, *J. Phys. Chem. Solid*, 146 (2020) 109569.
25. J. Li, S. Huang, S. Li, S. Xu, and C. Pan, *Ceram. Int.*, 43 (2017) 1650.
26. T. Ohzuku, A. Ueda, and N. Yamamoto, *Soc.*, 142 (1995) 1431.
27. J. P. Zhu, G. Yang, J. J. Zhao, Q. S. Wang, and H. W. Yang, *Adv. Mater. Research*, 279 (2011) 77.
28. H. Roh, G. Lee, S. Haghghat-Shishavan, K. Y. Chung, K. B. Kim, *Chem. Eng. J.*, 385 (2020) 123984.
29. B. Gangaja, S. Nair, and D. Santhanagopalan, *Appl. Surf. Sci.*, 480 (2019) 817.
30. Y. Lin, J. Wu, X. Huang, G. Pan, and X. Xia, *J. Energy Chem.*, 51 (2020) 372.
31. C. Jiang, Z. Ye, H. Ye, and Z. Zou, *Appl. Surf. Sci.*, 504 (2020) 144464.
32. I. A. Stenina, A. N. Sobolev, A. A. Kuz'Mina, T. L. Kulova, A. M. Skundin, N. Y. Tabachkova, and A. B. Yaroslavtsev, *Inorg. Mater.*, 53 (2017) 1039.
33. H. Wang, S. Li, Y. Yang, W. Yu, Q. Ma, X. Dong, J. Wang, and G. Liu, *Russ. J. Phys. Chem. A.*, 93 (2019) 144.